The final publication is available at

http://dx.doi.org/10.1002/smll.201401227

Additional Information

Towards the development of smart 3D "gated scaffolds" for on-command delivery

Núria Mas, Daniel Arcos, Lorena Polo, Elena Aznar, Sandra Sánchez-Salcedo, Félix Sancenón, Ana García, M. Dolores Marcos, Alejandro Baeza, María Vallet-Regí, and Ramón Martínez-Máñez**

N. Mas, Lorena Polo, Dr. E. Aznar, Dr. Félix Sancenón, Dr. M.D. Marcos and Prof. R. Martínez-Máñez,
Centro de Reconocimiento Molecular y Desarrollo Tecnológico (IDM). Unidad Mixta Universitat de València – Universitat Politècnica de València and Departamento de Química. Camino de Vera s/n, 46022, Valencia, Spain and CIBER de Bioingeniería, Biomateriales y Nanomedicina (CIBER-BBN), Spain.
E-mail: rmaez@qim.upv.es

Dr. D. Arcos, Dr. S Sánchez-Salcedo, Dr. A. García, Dr. A. Baeza and Prof. M. Vallet-Regí, Departamento de Química Inorgánica y Bioinorgánica. Facultad de Farmacia, Universidad Complutense de Madrid. Instituto de Investigación Sanitaria Hospital 12 de Octubre i+12. Plaza Ramón y Cajal s/n, 28040 Madrid, Spain, and CIBER de Bioingeniería, Biomateriales y Nanomedicina (CIBER-BBN), Spain.
 E-mail: vallet@farm.ucm.es

Porous biomaterials using polymers, ceramics, metals, or glasses, have been extensively

studied, and are widely used as scaffolds for tissue and bone regeneration in a multi-

millionaire market context.[1,2] Porous scaffolds provide a three-dimensional environment that

preserves tissue volume, supports cell interactions and, in some cases, delivers biological

agents for repairing, maintaining, restoring or improving the function of organs and tissues.[3]

In all these cases, it is highly desirable to have scaffolds that can regulate the delivery of

biological agents (for instance, drugs, cells, etc.) because control over release can improve the

safety and efficiency of agents, and allows the design of advanced scaffolds and new therapies.

However, most of the porous scaffolds currently used in tissue engineering are mainly non-

active; that is, they deliver biological agents through passive mechanisms which typically

involve material degradation coupled with molecular diffusion.[4-11] Moreover, the drug

release kinetics of these systems is usually uncontrolled and supports are unable to retain the drug payload for a long time.[12]

From a different point of view, progress in bio-molecular chemistry and nanotechnology have recently resulted in the design of biologically inspired systems with innovative bio-related functions and fuelling areas, such as bio-engineering, bio-sensing, bio-nanotechnology and drug delivery in new directions. Drug-delivery systems capable of releasing active molecules in a controlled manner have recently gained much attention. In this field, mesoporous silica nanoparticles (MSN) have been widely used as reservoirs for drug storage given their unique mesoporous structure, large specific volume and easy functionalisation.[13] Additionally, MSN can be functionalised with molecular/supramolecular ensembles on their external surface to develop gated MSN which show "zero delivery" (i.e., the hybrid material is unable to release the payload), but are capable of releasing their cargo in response to external stimuli.[14-18] The great potential of designing a hybrid material with nanometric controlled delivery features has motivated scientists to develop a wide variety of stimuli-responsive MSN-capped systems capable of being opened by chemical[19-25] (i.e., redox molecules, selected anions, pH changes and biomolecules), physical[26-31] (i.e., light, temperature or magnetic fields) or biochemical[32-37] triggers.

Given the need to develop scaffolds for advanced therapies which can improve features of conventional systems, in this communication, we show for the first time (as far as we are aware) a new approach to design tailor-made scaffolds capable of displaying selective and controlled cargo delivery based on the combination of suitable 3D supports and gated mesoporous materials. As a proof of concept, our strategy involves the preparation of a biomaterial of potential application in bone tissue engineering. It consists of a macroporous scaffold, prepared by rapid prototyping (RP) techniques, that incorporates capped MSN designed to deliver the cargo under specific events. In particular, the designed MSN can be opened on command in the presence of acid phosphatase (APase), an enzyme whose

2

concentration is used to assess osteoclast activity in bone remodelling processes[38-39] and as a biochemical marker for the presence of bone metastases.[40,41] Accordingly, this stimuli-responsive "gated scaffold" opens up new alternatives to treat osteoporotic fractures and bone cancer.
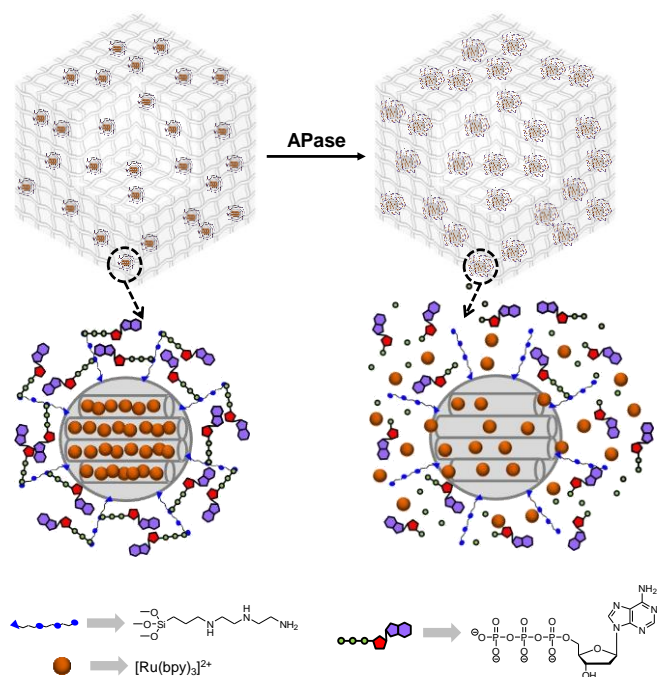
Scheme 1. Schematic representation of the APase-driven MSN system.

For this study, MCM-41-based MSN (ca. 100 nm) were selected as the inorganic scaffold. Calcined MSNs were loaded with tris(2,2'-bipyridyl)ruthenium(II) chloride and the external surface of the silica mesoporous nanospheres was functionalised with 3-[2-(2-aminoethylamino)ethylamino]propyl-trimethoxy silane to yield solid **S1**. The final material (solid **S2**) was obtained by treating the neutral aqueous solutions of **S1** with adenosine triphosphate (ATP). This is expected to cap the pores by the formation of a dense network in pore outlets through supramolecular hydrogen-bonding interactions, and electrostatic forces between the large negatively charged ATP anions and the positively charged ammonium groups on MSN. The presence of ATP in **S2** would inhibit cargo release, whereas the hydrolysis of the ATP cap by APase is anticipated to induce it, as depicted in **Scheme 1**.

The calcined starting MSN and solids **S1** and **S2** were characterised by standard techniques. **Figure 1A** shows the diffraction pattern of the prepared solids, which display typical features of the MCM-41 phase, indicating that the mesopores in the nanoparticles were preserved throughout the filling process, external amines anchoring and capping with ATP. **Figure 1B** depicts a representative TEM image of solid **S2**, in which the black and white strips, typical of the porosity of the MCM-41 phase, can be clearly seen.
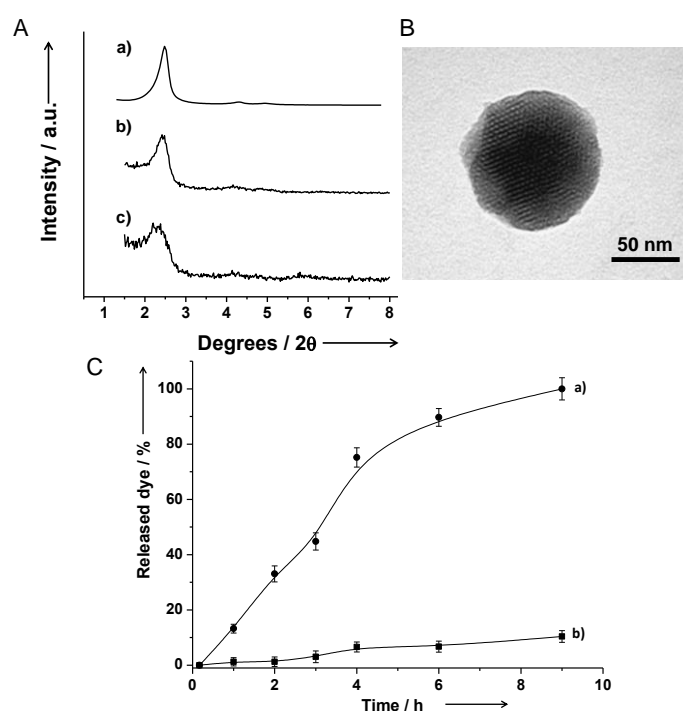

Figure 1. (A) Powder X-Ray diffraction pattern of a) starting calcined MCM-41, b) nanoparticulated **S2**, c) **S3** scaffold (vide infra). (B) Representative TEM image of the **S2** gated nanoparticles. (C) Kinetic dye release studies done at 37°C in water of ATP-capped solid **S2** a) in the presence and b) absence of APase.

The N_2 adsorption-desorption isotherm of the starting calcined MSN showed a typical type-IV curve from which a specific surface area of 931.5 m^2g^{-1}, a narrow pore size distribution and an average pore diameter of 2.39 nm were calculated. In contrast, the N_2 adsorption-desorption isotherm of final gated materials **S2** was typical of the capped and filled

4

mesoporous systems. In this case, a lower N_2 adsorbed volume and a smaller surface area (24.6 m^2g^{-1}) were found when compared with the starting material (see Supporting Information for further details). Moreover, the organic content of solids **S1** and **S2** calculated from thermogravimetry and elemental analysis are shown in Table 1.

Table 1. Organic content (α, mmol/g of solid) in solids **S1** and **S2**

	α_{dye}	$\alpha_{polyamine}$	α_{ATP}
S1	0.16	1.70	--
S2	0.04	1.35	0.14

After characterisation, cargo release studies were carried out with **S2**. In a typical experiment, 4 mg of **S2** were suspended in water in both the presence and absence of APase. Suspensions were kept at 37ºC, and at certain time intervals, fractions of both suspensions were taken and centrifuged to remove the solid. Dye delivery into the solution was then measured by the fluorescence of $[Ru(bpy)_3]^{2+}$ at 593 nm (λ_{ex} 454 nm). The delivery profiles of $[Ru(bpy)_3]^{2+}$ in both the presence and absence of APase enzyme are shown in **Figure 1C**. As seen, nanoparticles **S2** are tightly capped in the absence of APase and show a negligible release of $[Ru(bpy)_3]^{2+}$ (**Figure 1C**, curve b); in contrast, the presence of APase induces the opening of the pores and the subsequent cargo release.

The observed performance confirms the proposed paradigm. When APase enzyme is absent, ATP molecules interact strongly with the polyamines anchored in **S2** and are able to block the release of the entrapped dye. However in the presence of APase, the enzyme hydrolyses the phosphate-phosphate ATP bonds by disassembling the polyamine-phosphate interactions, and by inducing the pore aperture and the subsequent dye release. The APase-mediated hydrolysis of ATP in **S2** was confirmed by STEM-EDX studies which, in turn, confirmed that the P/Si ratio in **S2** was 3-fold lower when the solid was treated with APase. Moreover ^{31}P-NMR studies done in the aliquots collected in the release studies clearly showed the presence of

increasing amounts of phosphate (at δ +2.1 ppm), which correlated well with the amount of released cargo. Finally, in order to further confirm that the uncapping mechanism was driven by APase, dye release studies on **S2** in the presence of other enzymes, such as esterase and pepsin, and in the presence of denatured APase, were performed. Under these conditions, no significant cargo release was observed (see Supporting Information).

Bearing in mind the promising results obtained with capped solid **S2**, we take a step forward towards the possibility of designing gated 3D macroporous scaffolds for potential applications for filling bone defects. In these designed supports, the scaffold macropore system must be highly interconnected and large enough to support bone ingrowth and angiogenesis. Depending on the kind of the host bone, i.e. cortical or cancellous bone, these parameters can vary, but the pore size must be large enough to allow the formation of mature bone within the macropore arrangement, being considered an appropriate pore size a range between 300-2000 micrometers for the bone ingrowth after implantation.[45,46] In this context many processes have been developed to prepare macroporous supports, such as replicas of porous sponges and coral exoskeletons, production of gas bubbles via gas evaporation, chemical reactions, and introduction of porogens (such as organic volatile particles) in a ceramic slip and gel-casting, either alone or in combination with a multiple tape-casting method.[42-44] However, pore size, shape and its interconnectivity, cannot be fully controlled in these approaches. In contrast, rapid prototyping (RP) is a good alternative to fulfil requirements for manufacturing suitable scaffolds for different clinical applications and individuals. Following these concepts, the **S2** nanoparticles were incorporated into a 3D gelatin framework produced using rapid prototyping 3D printing[40,41] to obtain the final gated 3D scaffold **S3**.

In a typical experiment to prepare **S3**, an aqueous solution of gelatin at 37ºC was mixed with **S2** nanoparticles under vigorous stirring. Then a solution containing glutaraldehyde as a cross-linker was added. The mixture was stirred at room temperature until it formed a paste of appropriate consistency for injection. The scaffold was fabricated by direct ink deposition

over a pre-cooled plate to build 3D-pieces with tetragonal symmetry. After frizzing samples, they were cut into smaller ca. 6×6×4 mm new dimensions, and were once again placed in a glutaraldehyde solution. Finally after a new freeze and drying process, **S3** was obtained.

The **S3** gated scaffolds were characterised by X-ray diffraction (XRD), thermogravimetry and SEM. The presence of the (100) reflection in the **S3** XRD pattern (**Figure 1Ac**) confirmed mesostructure preservation during the scaffold manufacturing process. From the thermogravimetric analysis, a content of 25±3% in weight of SiO_2 was calculated. It is estimated that around 35% in weight of **S3** is composed of **S2** nanoparticles. The SEM analysis of the **S3** scaffolds showed several porosity levels, resulting in a hierarchical porous system. At the macroscopic level, **S3** presented orderly distributed pores from 900 to 1200 µm, which are the product of the porosity architecture designed by the rapid prototyping of the scaffold surface and the scaffold fracture, respectively (**Figure 2A** and **B**). A second porosity level is also observed (**Figure 2C** and **D**) in the sinus of the scaffold walls. This second level is formed by pores from 40-100 µm, whose size and presence are determined by the degree of cross-linking of the gelatin. This macroporosity makes the permeability of the surrounding medium possible (in which the APase can be included) in the inner scaffold walls. Finally, the images taken at higher magnifications (**Figure 2D** and **E**) show a sponge-like structure formed by gelatin covers that surrounds the **S2** nanoparticles. The observed scaffold features were also studied by EDX analysis, which was performed at several **S3** sites (**Figure 2F**). The presence of Si and P in the magnified images of **S3** confirmed the incorporation of the **S2** nanoparticles into the scaffold. Moreover, in vitro degradability of **S3** in water was studied. In a typical experiment, a piece of 8 mg of **S3** was placed in 1 mL of distilled water under orbital stirring at 37 ºC. The weight of the hydrated scaffolds was measured after ten months and only a 10 % of weight lost was observed.
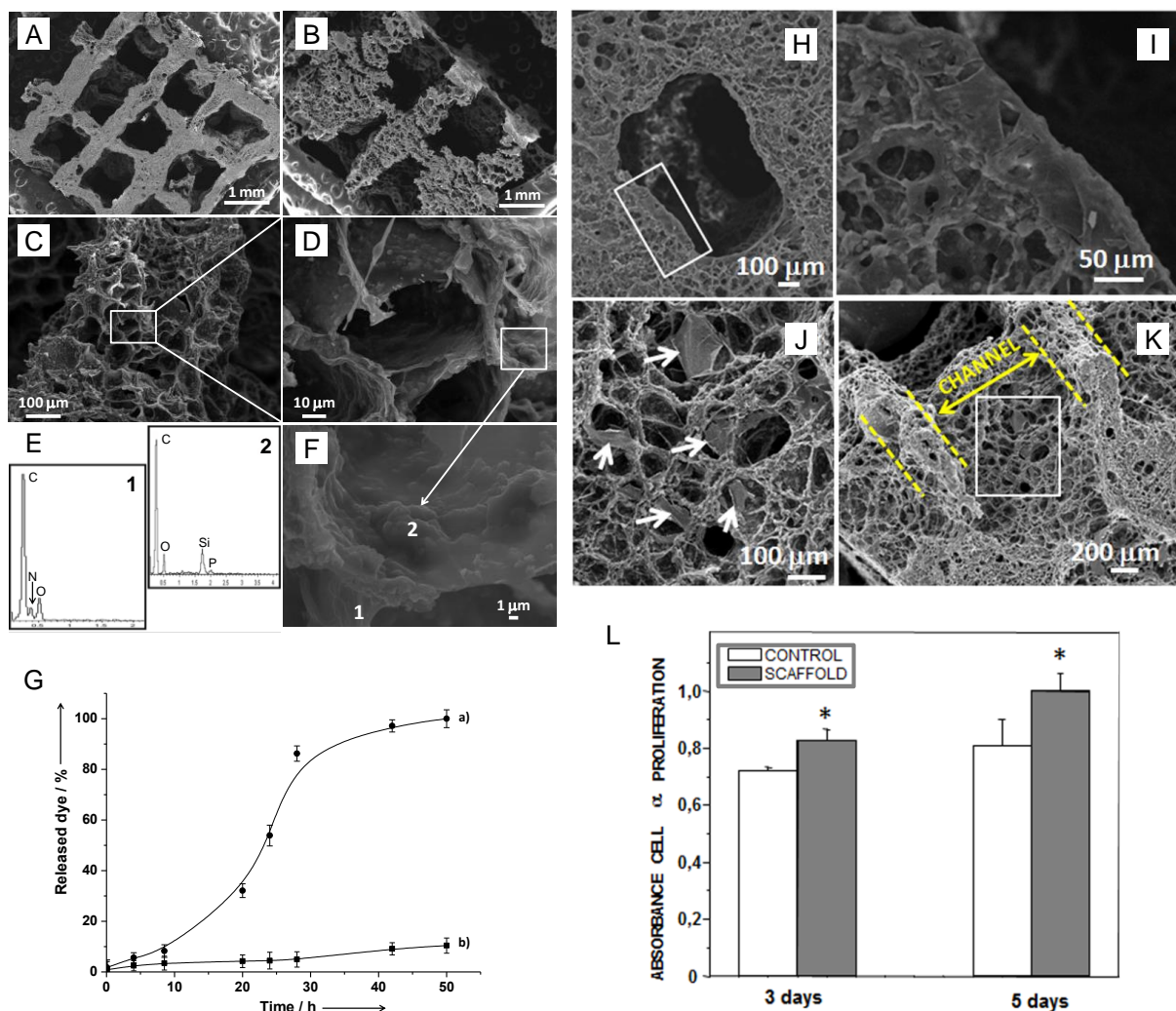
Figure 2. (A) SEM Image at low magnifications of the **S3** surface and (B) the **S3** fracture, showing giant macroporosity. (C) Image of **S3** at high magnifications in which a second porosity level can be observed due to the gelatin cross-linking, (D) second macroporosity level showing the incorporated **S2** nanoparticles. (E) Higher magnification shows a wall scaffold with embedded **S2** nanoparticles. (F) EDX microanalysis of image E at sites 1 (wall) and 2 (**S2** nanoparticles). (G) Dye release kinetics in PBS at 37ºC from **S3** (a) in the presence and (b) absence of APase. SEM micrographs of the scaffolds after 48 hours of HOS culture. (H) Detail of c.a. 900 µm macropore prepared by 3D printing. The selected area indicates a fully coated border site by HOS cells; higher magnification of this area (I). (J) Transversal section of the scaffolds; double arrow points the channel width and dotted lines mark the struts. The selected area is magnified in (K), where spread HOS cells can be observed

(arrows).(L) Cell proliferation assay after 3 and 5 days of culture. Significant differences were observed between the control and scaffolds results for cell proliferation tests. *(p<0.05).

Then release studies were performed. In a typical experiment, "gated scaffold" **S3** was immersed in a PBS solution in the presence and absence of APase. Both solutions were stirred for 50 h at 37ºC and, at a set time, an aliquot of each experiment was taken to monitor cargo release. The obtained results are shown in **Figure 2G**. As observed, delivery was found only when the enzyme was present, thus confirming that the APase-driven release mechanism found for **S2** was maintained in the **S3** scaffold. Slower release kinetics was also found for **S3** when compared with **S2**, most probably due to the enzyme's different accessibility to the hierarchical hybrid structure in the gated scaffold when compared with free nanoparticles. The permeability of these 3D scaffolds to large macromolecules was confirmed after placing them in a solution with fluorescein-labelled avidin macromolecules as an enzyme model. After 1 day, scaffolds were sliced into thin films and intense fluorescence was observed in all the pieces (see Supporting Information). As far as we know, this is the first example of gated scaffolds obtained by combining biomaterials and gated stimuli-controlled nanoparticles. Finally, in order to assess the biocompatibility of the scaffold, *in vitro* cell culture tests were carried out on 3D gelatin framework containing silica nanoparticles. For that pourpose, a human osteoblast-like cell line denoted HOS was used. Cell proliferation, cytotoxicity and spreading assays were performed (see Supporting Information for further details). In these experiments (see **Figure 2L**) it was found that HOS cells proliferate even better than in the control (plastic culture plate), and the LDH levels do not show significant differences in the presence of the scaffolds compared with the control ones, indicating that the scaffolds do not elicit any cytotoxic effect. Finally, SEM micrographs (see **Figures 2H-K**) confirmed that HOS cells adhere, proliferate and spread well within the scaffold, confirming that the

macroporous architecture and the strut thickness is appropriated for the scaffold colonization by HOS cells.

In summary, we report herein a new approach for the design of "gated scaffolds" which consists in combining capped silica mesoporous nanoparticles and classical porous biomaterials. In particular, we have prepared MSN functionalised with amines and capped with ATP, which can be selectively opened with an APase enzyme. We have also integrated capped nanoparticles into a 3D gelatin support prepared by rapid prototyping 3D printing techniques. The obtained "gated scaffold" remains tightly capped in competitive aqueous buffered solutions yet is able to deliver the cargo in the presence of APase. The present study has focused on the capability of active gelatin-based 3D macroporous scaffolds for on-command cargo delivery in the presence of APase, an enzyme whose concentration is used to assess osteoclast activity in bone remodelling processes and as a marker for bone metastases. We also expect this general gated scaffolds preparation approach, will find broader applications. In particular, the combination of gated nanoparticles, which can be opened at will using chemical, physical or biochemical stimuli with different supports based on polymers, ceramics or metals, opens up the possibility of preparing a number of advanced gated scaffolds, which we envision can help find applications in regenerative medicine and bone cancer therapy.

Supporting Information
Supporting Information is available from the Wiley Online Library or from the author.

10

[1]   V. Karageorgiou, D. Kaplan, *Biomaterials*, **2005**, *26*, 5474–5491.

[2]   Q.L. Loh, C. Choong, *Tissue Eng Part B* **2013**, *19*, 485–502.

[3]   M. Vallet-Regí, E. Ruíz-Hernández, *Adv. Mater.* **2011**, *23*, 5177–5218.

[4]   K. Whang, T.K. Goldstick, K.E. Healy, *Biomaterials* , **2000**, *21*, 2545-255.

[5]   J.W. Lee, K. Shin Kang, S. Ho Lee, J.-Y. Kim, B.-K. Lee, D.-W. Cho, *Biomaterials*, **2011**, *32*, 744-752.

[6]   C.-X. He, N. Li, Y-L. Hu, X.-M. Zhu, H.-J. Li, M.-H., P.-H. Miao, Z.-J. Hu, G. Wang, W.-Q. Liang, Y. Tabata, J.-Q. Gao*, Pharm Res*, **2011**, *28*,1577–1590.

[7]   S. Kedong, L. Yingchao, H. M. Macedo, J. Lili, L.Chao, M. Guanyu, L. Tianqing, *Mater.Sci.Eng. C*, **2013**, *33*, 1506–1513.

[8]   J. Hu, P. X. Ma, *Pharm Res,* **2011**, *28*, 1273–1281.

[9]   G. Poologasundarampillai, B. Yu, O. Tsigkou, E. Valliant, S. Yue, P. D. Lee, R. W. Hamilton, M. M. Stevens, T. Kasugad and J. R. Jones, *Soft Matter*, **2012**, *8*, 4822–4832.

[10]   L. S. Sefcik, C. E. Petrie Aronin, K. A. Wieghau, E. A. Botchwey, *Biomaterials*, **2008**, *29*, 2869–2877.

[11]   Q. Peng, Y.-J.Yang, T. Zhang, C.-Y. Wu, Q. Yang, X. Sun, T. Gong, L. Zhang, Z.-R. Zhang, *Pharm Res,* **2013**, *30,* 1077–1085.

[12]   W. Habraken, J.G.C. Wolke, J.A. Jansen JA., *Adv. Drug Deliv. Rev.*, **2007**, *59*, 234–248.

[13]   M. Vallet-Regí, F. Balas, D. Arcos, *Angew. Chem.* **2007**, *119*, 7692 – 7703; *Angew. Chem. Int. Ed.* **2007**, *46*, 7548 – 7558.

[14]   J. L. Vivero-Escoto, I. I. Slowing, B. G. Trewyn, V. S.-Y. Lin, *Small* **2010**, *6*, 1952 – 1967.

[15]   P. Yang, S. Gai, J. Lin, *Chem. Soc. Rev,* **2012**, *41*, 3679-3698.

[16]   Z. Li, J.C. Barnes, A. Bosoy, J. F. Stoddart, Zink. *Chem. Soc. Rev*, **2012**, *41*, 2590-2605.

[17]   B. G. Trewyn, I. I. Slowing, S. Giri, H. –T. Chen, V. S. –Y. Lin, *Acc. Chem. Res.*, **2007**, *40*, 846-853.

[18]   C. Coll, A. Bernardos, R. Martínez-Máñez, F. Sancenón, *Acc. Chem. Res.* **2013**, *46*, 339 – 349.

[19]   C.-Y Lai, B.G. Trewyn, D.M. Jeftinija, K. Jeftinija, S. Xu, S. Jeftinija, V. S. –Y. Lin, *J. Am. Chem. Soc.* **2003**, *125*, 4451

[20]   C. Park, K. Oh, S.C. Lee, C. Kim, *Angew. Chem. Int. Ed.* **2007**, *46*, 1455.

[21]   R. Liu, X. Zhao, T. Wu, P. Feng, *J. Am. Chem. Soc.*, **2008**, *130*, 14418-14419.

[22]   Z. Luo, K. Cai, Y. -Hu, L. Zhao, P. Liu, L. Duan, W. Yang, *Angew. Chem.* **2011**, *123*, 666 – 669; *Angew. Chem. Int. Ed.* **2011**, *50*, 640 – 643.

[23]   C. Wang, Z. Li, D. Cao, Y.-L. Zhao, J. W. Gaines, O. A. Bozdemir, M.W. Ambrogio,M. Frasconi, Y. Y. Botros, J. I. Zink,J. F. Stoddart, *Angew. Chem*. **2012**, *124*, 5556 – 5561; Angew. Chem. Int. Ed. **2012**, *51*, 5460 – 5465.

[24]   a) Y. Zhang, Q. Yuan, T. Chen, X. Zhang, Y. Chen, W. Tan, *Anal. Chem.* **2012**, *84*, 1956 – 1962; b) D. Tarn, M. Xue, J. I. Zink, *Inorg. Chem.* **2013**, *52*, 2044 – 2049.

[25]   a) E. Climent, R. Martínez-Máñez, A. Maquieira, F. Sancenón, M.D. Marcos, E.M. Brun, J. Soto, P. Amorós, *ChemistryOpen* **2012**, *1*, 251 – 259; b) E. Aznar, R. Villalonga, C. Giménez, F. Sancenón, M.D. Marcos, R. Martínez-Máñez, P. Díez, J.M. Pingarrón, P. Amorós, *Chem. Commun.* **2013**, *49*, 6391 – 6393.

[26]   N. K. Mal, M. Fujiwara, Y. Tanaka, *Nature*, **2003**, *421*, 350-353.

[27]   A. Schlossbauer, S. Warncke, P. M. E. Gramlich, J. Kecht, A. Manetto, T. Carell, T. Bein, *Angew. Chem*. **2010**, *122*, 4842 – 4845; *Angew. Chem. Int. Ed.* **2010**, *49*, 4734 – 4737.

[28]   E. Ruiz-Hernández, A. Baeza, M. Vallet-Regi, *ACS Nano* **2011**, *5*, 1259 – 1266.

[29]   D. He, X. He, K.Wang, J. Cao, Y. Zhao, *Adv. Funct. Mater.* **2012**, *22*, 4704 – 4710.

[30]   E. Aznar, L. Mondragón, J.V. Ros-Lis, F. Sancenón, M.D. Marcos, R. Martínez-Máñez, J. Soto, E. Pérez-Payá, P. Amorós, *Angew. Chem. Int. Ed.* **2011**, *50*, 11172.

[31]   A. Baeza, E. Guisasola, E. Ruiz-Hernández, M. Vallet-Regi, *Chem. Mater.* **2012**, *24*, 517 – 524.

[32]   A. Schlossbauer, J. Kecht, T. Bein, *Angew. Chem.* **2009**, *121*, 3138 – 3141; *Angew. Chem. Int. Ed.* **2009**, *48*, 3092 – 3095

[33]   C. Park, H. Kim, S. Kim, C. Kim, *J. Am. Chem. Soc*. **2009**, *131*, 16614 – 16615.

[34]   A. Bernardos, L. Mondragón, E. Aznar, M.D. Marcos, R. Martínez-Máñez, F. Sancenón, J. Soto, J. M. Barat, E. Pérez-Payá, C. Guillem, P. Amorós, *ACS Nano* **2010**, *4*, 6353 –6368.

[35]   P. D. Thornton, A. Heise, *J. Am. Chem. Soc.*, **2010**, *132*, 2024-2028.

[36]   A. Popat, B. P. Ross, J. Liu, S. Jambhrunkar, F. Kleitz, S. Z. Qiao, *Angew. Chem.* **2012**, *124*, 12654 – 12657; *Angew. Chem. Int. Ed.* **2012***, 51*, 12486 – 12489.

[37]   a) Z. Chen, Z. Li, Y. Lin, M. Yin, J. Ren, X. Qu, *Chem. Eur. J.* **2013**, *19*, 1778 – 1783; b) L. Mondragón, N. Mas, V. Ferragud, C. de la Torre, A. Agostini, R. Martínez-Máñez, F. Sancenón, P. Amorós, E. Pérez-Payá, M. Orzáez, *Chem. Eur. J.* **2014**, *20*, 5271 – 5281.

[38]   C. Minkin, *Calcified Tissue Int.,* **1982**, *34*, 285–290.

[39]   J.S. Hanker, A.D. Dixon, G.R. Smiley, *Histochemie*, **1973**, *35*, 39-50.

[40]   M. Tavassoli, M. Rizo, L.T.Yam. *Cancer*, **1980**, *45*, 2400-2403.

[41]   N. Wadu, S. Ishii, T. Ikeda, K. Enomoto, M. Kitajima. *Anticancer Res* **1999**, 19, 4515-4521.

[42]   R.P. del Real, J.G.C. Wolke, M. Vallet-Regí, J.A. Jansen, *Biomaterials*, **2002**, *23*, 3673–3680.

[43]   S. Padilla, S. Sánchez-Salcedo, M. Vallet-Regí, *J. Biomed. Mater. Res.*, **2007**, *81A*, 224–232.

[44]   S. Sánchez-Salcedo, J. Werner, M. Vallet-Regí, *Acta Biomater.,* **2008**, *4*, 913–922.

[45]   V. Karageorgiou, D. Kaplan, *Biomaterials*, **2005**, *26*, 5474–5491.

[46]   L. Guan, J.E. Davies, *J. Biomed. Mater. Res.*, **2004**, *71A*, 480–487.

A new approach towards the design of "gated scaffolds" based on the combination of capped mesoporous silica nanoparticles (MSN) with porous biomaterials is reported. Using this approach, a 3D gelatin-based scaffold able to selectively deliver cargo in the presence of an APase enzyme is prepared and tested. This new design opens up the possibility of developing new smart biomaterials with advanced drug delivery features.

Gated biomaterials

Núria Mas, Daniel Arcos, Elena Aznar, Sandra Sánchez-Salcedo, Félix Sancenón, Ana García, M. Dolores Marcos, Alejandro, Baeza, María Vallet-Regí*, and Ramón Martínez-Máñez*

Towards the development of smart 3D "gated scaffolds" for on-command delivery
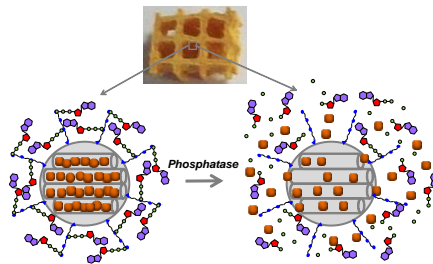
Supporting Information

Towards the development of 3D "gated scaffolds" for on-command delivery

Núria Mas, Daniel Arcos, Lorena Polo, Elena Aznar, Sandra Sánchez-Salcedo, Félix Sancenón, Ana García, M. Dolores Marcos, Alejandro Baeza, María Vallet-Regí*, and Ramón Martínez-Máñez*

Chemicals

The chemicals tetraethylorthosilicate (TEOS) (98 %), n-cetyltrimethylammonium bromide (CTAB) (≥99 %), sodium hydroxide (≥98 %), tris(2,2'-bipyridyl)ruthenium(II) chloride hexahydrate, 3-[2-(2-aminoethylamino)ethylamino]propyl-trimethoxysilane, adenosine 5'-triphosphate disodium salt hydrate (ATP), acid phosphatase from potato (APase), gelatin Ph Eur and glutaraldehyde 50 wt.% solution in water where purchased from Aldrich. $Na_2HPO_4 \cdot 7H_2O$, KH_2PO_4 , NaCl and KCl where purchased from Scharlab. All reagents were used as received.

General Techniques

Powder XRD, TG analysis, ele-mental analysis, TEM, SEM, zeta potential measurements, and N_2 adsorption-desorption techniques were employed to characterize the prepared materials. Powder X-ray diffraction measurements were performed on a Philips D8 Advance diffractometer using Cu Kα radiation. Thermogravimetric analysis were carried out on a TGA/SDTA 851e Mettler Toledo balance, using an oxidant atmosphere (air, 80 mL/min) with a heating program consisting on a heating ramp of 10^0C per minute from 393 to 1273 K and an isothermal heating step at this temperature during 30 minutes. Elemental analysis was performed in a CE Instrument EA-1110 CHN Elemental Analyzer. TEM images were obtained with a 100 kV Jeol JEM-1010 microscope. Z potential measurements were

performed in a Zetasizer Nano instrument from Malvern. N_2 adsorption-desorption isotherms were recorded on a Micromeritics ASAP2010 automated sorption analyser. The samples were degassed at 120^0C in vacuum overnight. The specific surface areas were calculated from the adsorption data in the low pressures range using the BET model. Pore size was determined following the BJH method. STEM analysis was performed with a 200kV Jeol JEM 2100F. ^{31}P nuclear magnetic resonance (NMR) was acquired with a Brucker Avance III. Surface and cross-sectional scanning electron microscopy (SEM) micrographs of **S3** and EDX analysis of the scaffolds were recorded with a field emission scanning electron microscope (JEOL model JSM-6335, Tokyo, Ja-pan) at an acceleration voltage of 15 kV. For scaffolds manufacture, an EnvisionTEC GmbH 3-D Bioplotter™ was used. In release experiments, fluorescence spectroscopy was carried out with a Jasco Spectrofluorometer FP-8500.

Synthesis of the mesoporous silica support

The MCM-41 mesoporous nanoparticles were synthesised by the following procedure: n-cetyltrimethylammonium bromide (CTAB, 1.00 g, 2.74 mmol) was first dissolved in 480 mL of deionised water. Then 3.5 mL of NaOH 2.00 M in deionised water were added to the CTAB solution. Next, the solution temperature was adjusted to 80°C. TEOS (5.00 mL, 2.57×10^{-2} mol) was then added dropwise to the surfactant solution. The mixture was stirred for 2 h to give a white precipitate. Finally, the solid product was centrifuged, washed with deionised water and ethanol, and was dried at 60°C (MCM-41 as-synthesised). To prepare the final porous material (MCM-41), the as-synthesised solid was calcined at 550°C using an oxidant atmosphere for 5 h in order to remove the template phase, obtaining the porous material.

Synthesis of S1.

In a typical synthesis, 2.5 g of template-free MCM-41 were suspended in a solution of 1.5 g (2 mmol) of tris(2,2'-bipyridyl)ruthenium(II) chloride hexahydrate ($[Ru(bpy)_3]^{2+}$) dye in 80

mL of anhydrous acetonitrile in a round-bottomed flask. Then 10 ml of acetonitrile were distilled with a dean-stark, in order to remove the possible water present in the pores of the solid. Afterwards the mixture was stirred at room temperature during 24 hours. Subsequently, 10 mL (15 mmol/g of MCM-41) of 3-[2-(2-aminoethylamino)ethylamino]propyl-trimethoxysilane were added and the mixture was stirred for 5.5 h. Then the solid was filtered, washed with 10 mL of acetonitrile and dried at 37°C overnight to obtain the functionalised and filled solid **S1**.

Synthesis of S2

2.5 g of the loaded and prefunctional-ised solid **S1** were suspended in a solution 0.01 M of ATP at pH 6 adjusted with H_2SO_4. This suspension was stirred for 5.5 hours at room temperature and then filtered under vacuum and washed with water at pH 6. This final solid **S2** was dried under vacuum and stored at 37°C for 12 h.

Synthesis of S3

Gated MSN-scaffolds were prepared using **S2** nanoparticles. In particular, 0.5 g of gelatin were dissolved in 3.75 mL of milli-Q water at 37°C. Thereafter, 0.3 g of **S2** were slowly added under vigorous stirring. Once all the NPs were added, the mixture was stirred for 40 min at 37°C. Finally, 2.50 mL of a glutaraldehyde as cross-linking solution 0.4% v/v was added. This mixture was stirred at room temperature until it formed a paste with appropriated consistency for injection. The paste was placed in polyethylene cartridge fixed with a dispensing tip of 0.51 mm (EFD-Nordson) internal diameter and the spacing between struts was set to 1.8 mm. The scaffolds were fabricated by direct ink deposition over a pre-cooled plate (10-15°C) by robocasting using an EnvisionTEC GmbH 3-D Bioplotter™. Each layer was 90° rotate to the next one, building 3D-pieces with tetragonal symmetry. The dimension of scaffolds was ca. $18 \times 18 \times 4$ mm and consisted of 15 layers. They were frozen at -80°C for

2 h and they were cut on smaller ca. $6 \times 6 \times 4$ mm new dimensions. The small scaffolds produced were then cross-linked by exposure to 10 mL of a 2.5% v/v glutaral-dehyde aqueous solution for 10 s. Finally, the scaffolds were freeze-dried at -80°C for 4 h. The final series obtained were called **S3**.

Calcined MCM-41, S1 and S2 characterization.

All the mesoporous nanoparticles were characterized following standard techniques. The powder X-ray diffraction (XRD) pattern of the different synthesized solids is shown in Figure SI-1. In relation to the siliceous MCM-41 nanoparticles as synthesized the four low-angle reflections typical of a hexagonal array, indexed as (100), (110), (200), and (210) Bragg peaks are shown (curve a). A significant displacement of 4Å of the (100) peak in the XRD pattern of the MCM-41 calcined nanoparticles is evident in the X-ray pattern of MCM-41 calcined, due to further condensation of silanol groups during the calcination step (curve b). Finally, the X-ray diffraction pattern of both functionalized solids S1 and S2 can be observed in curves c) and d), respectively. An intensity decrease and a broadening of the (110) and (200) reflections can be appreciated, related to a loss of contrast due to the filling of the pore voids with the $[Ru(bpy)_3]Cl_2 \cdot 6H_2O$ dye and the external surface functionalization. Even so, the intensity of the (100) peak in this pattern strongly indicates that the mesoporous structure of the MCM-41 scaffold has not been modified after the loading and functionalization processes in the final S2 material.
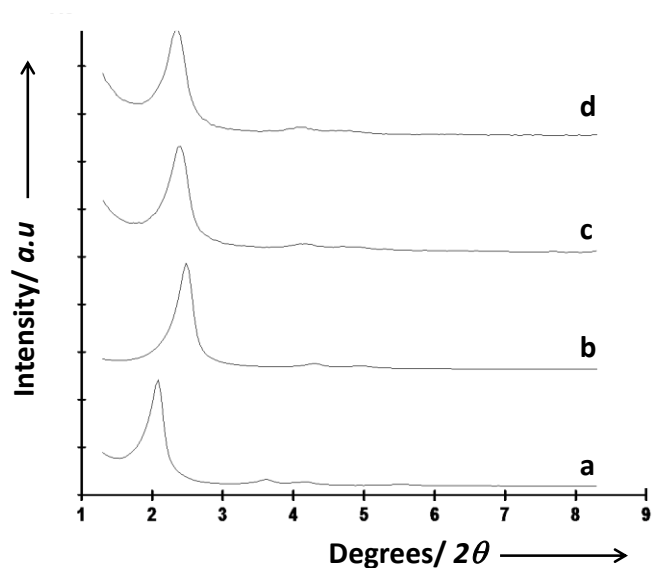
Figure SI-1. (A) Powder X-Ray pattern of (a) MCM-41 as made, (b) MCM-41 calcined and (c)

S1 solid and (d) **S2** solid.

Moreover, the presence of the mesoporous structure was confirmed by TEM analysis of the prepared solids. As it can be observed in **Figure SI-2**, the typical channels of the MCM-41 matrix can be visualised as alternate black and white stripes in which the typical hexagonal porosity of the MCM-41 calcined material can also be observed. TEM images also show that the prepared MCM-41-based support is obtained as spherical nanoparticles with diameters ranging from 80 to 100 nm. TEM image of the final solid **S2** (**Figure SI-2b**) also confirmed the ordered mesostructure of the final material. In that image, although the contrast between the black and white strips has decreased due to the loading of the pores with the dye, it can be confirmed that the spherical shape of the nanoparticles and their typical mesoporous structure remains.
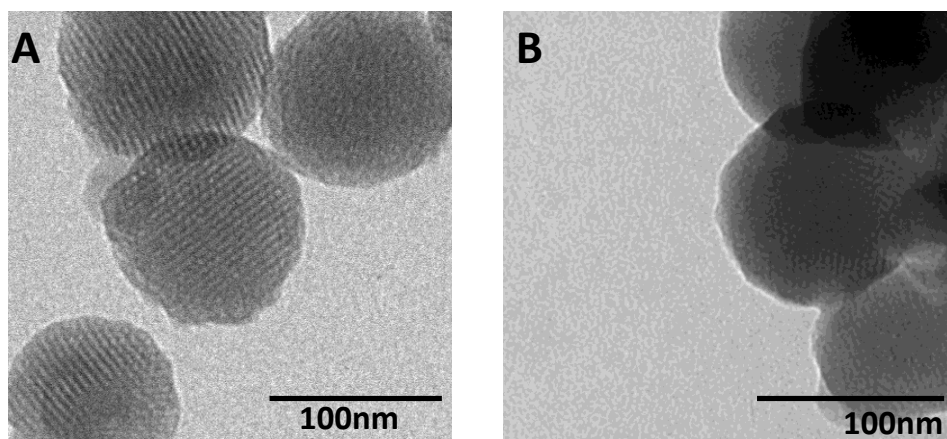
Figure SI-2. Representative TEM image of A) the inorganic MCM-41 calcined matrix. B) **S2** gated solid.

N_2 adsorption-desorption isotherms for calcined MCM-41 nanoparticles and the gated solid **S2** were registered and are shown in **Figure SI-3**. Curve a) corresponds to the calcined matrix showing a sharp adsorption step with a P/P_0 value between 0.2 and 0.35, corresponding to a type IV isotherm, typical of these mesoporous materials. This first step is due to nitrogen condensation in the mesopore inlets. With the BJH model on the adsorption curve of the isotherm, the pore diameter and pore volume were calculated to be 2.39 nm and 0.69 cm^3g^{-1}, respectively. The absence of a hysteresis loop in this pressure range and the low BJH pore distribution (see inset in **Figure SI-3**) is due to the cylindrical uniformity of mesopores. The total specific area was 931.5 m^2g^{-1}, calculated with the BET model. Also using the a_0 cell parameter 4.06 nm calculated form XRD measurements and the pore diameter (2.39 nm), a wall thickness value of 1.67 nm, was calculated. Other important feature of the curve is the characteristic H1 hysteresis loop that appears in the isotherm at a high relative pressure ($P/P_0 > 0.8$) which can be closely associated with a wide pore size distribution which corresponds to the filling of the large pores among the nanoparticles (0.69 cm^3g^{-1} calculated by the BJH model) due to textural porosity. In the case of the final **S2** material, the N_2 adsorption-desorption isotherm is typical of mesoporous systems with filled mesopores (see **Figure SI-3**, curve b). In this way, and as it was expected, a lower N_2 adsorbed volume (BJH mesopore

volume = 0.11 cm^{3}g^{-1}) and surface area (24.6 m^{2}g^{-1}) were determined, when compared with the initial MCM-41 material. As it can be observed in curve b, this solid presents a function with no gaps at low relative pressure values if compared to the mother MCM-41 array (curve a). A remarkable data is that **S2** did not show a maximum in the pore size distribution curve, which can be explained by the presence of closed pores because of the entrapped dye and the functionalization moieties in the external surface. Table SI-1 shows a summary of the BET-specific surface values, pore volumes and pore sizes calculated from the N$_2$ adsorption-desorption isotherms for MCM-41calcined and **S2**.
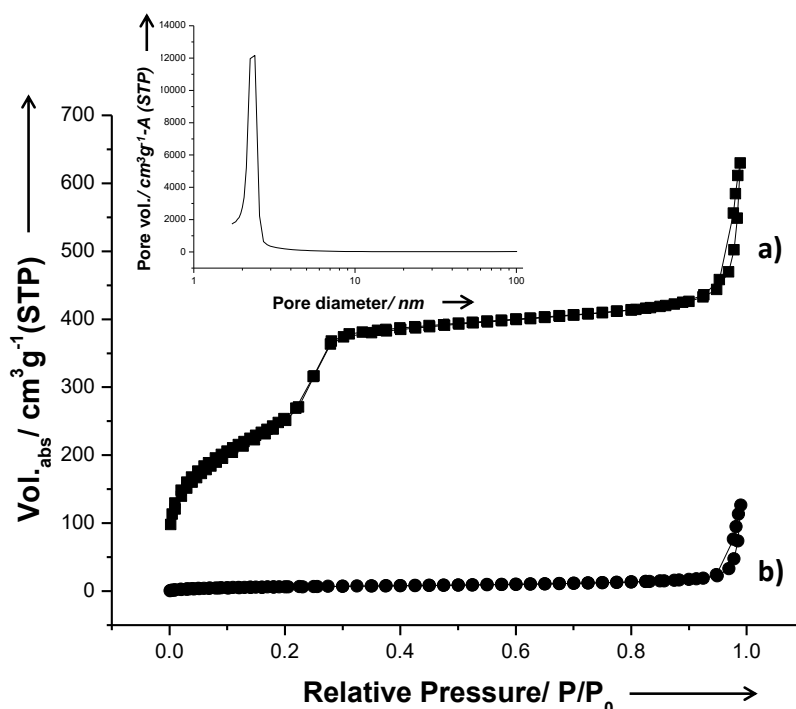

Figure SI-3. Nitrogen adsorption-desorption isotherms for (a) calcined MCM-41 mesoporous material (b) **S2**. Inset: Pore size distribution of calcined MCM-41 mesoporous material.

Table SI-1. BET specific surface values, pore volumes and pore sizes calculated from the N_2 adsorption-desorption isotherms for selected materials.

	S_{BET} (m^2g^{-1})	Pore Volume (cm^3g^{-1})	Pore Size (nm)
Calcined MCM-41	931.5	0.69	2.39
S2	24.6	0.11	-

Thermogravimetric studies of the final **S2** solid were also carried out. The thermogravimetric curve showed four weight losses steps which could be associated to the following processes: 7.00 % (T < 150 ^{0}C, corresponding to solvent removal), 14.9 % (150 < T < 400 ^{0}C, assigned to the decomposition of the organic moieties functionalizing the silica support), 12.8 % (400 < T < 550^{0}C, also due to combustion of organics) and 0.364 % (T > 550 ^{0}C, attributed to condensation of silanols in the siliceous surface).

The surface charge of the synthesized nanoparticles was characterized using a Malvern Zetasizer Nano ZS instrumentation. After appropriate dilution of the different suspensions of the nanoparticles, the parameters of electrophoretic mobility (EM), zeta potential (ζ) and conductivity (σ) were determined. Samples from the prepared suspensions were diluted in ultra-purified water and placed in the measurement cell. At least three different measurements were made for each sample. The final results obtained are shown in **Table SI-2**. MCM-41 calcined nanoparticles, showed a negative ζ value, due to the silanol groups present in the material's surface. In relation to the prefunctionalized solid **S1**, a strong change in the sign of potential was induced, making it clearly positive because of the positive charges of the polyamine

22

moieties. And finally, as it was expected, **S2** showed a low positive ζ value due to the presence of the ATP anions used as caps.

Table SI-2. Physicochemical properties of the prepared solids.

	EM (µm·cm/V·S)	ζ (mV)	σ (mS/cm)
MCM-41 calcined	-2.719±0.004	-34.7±0.6	0.0171
S1	2.695±0.007	34.4±1.1	0.0544
S2	1.409±0.002	17.9±0.2	0.0207

S3 characterization

Scaffold series were characterized by standard techniques such as X-ray diffraction (XRD), thermogravimetry and SEM. In relation to the XRD pattern at low angle, a low angle diffraction peak was registered which can be attributed to the (100) reflexion typical of the hexagonal lattice p6m of the MCM-41 materials (see **Figure SI-4**). This fact indicated that the incorporation of the MSN nanoparticles in the scaffolds did not affect at the mesoporous structure of **S2**. Despite, when MSN were incorporated in the gelatin scaffold, a significant decrease in (100) reflexion peak was observed. This can be explained by a resolution loss in the maximum diffraction peaks of the mesoporous nanoparticles because of high gelatin content in the scaffold or because of a small degree of structural defects created in the lyophilization process.
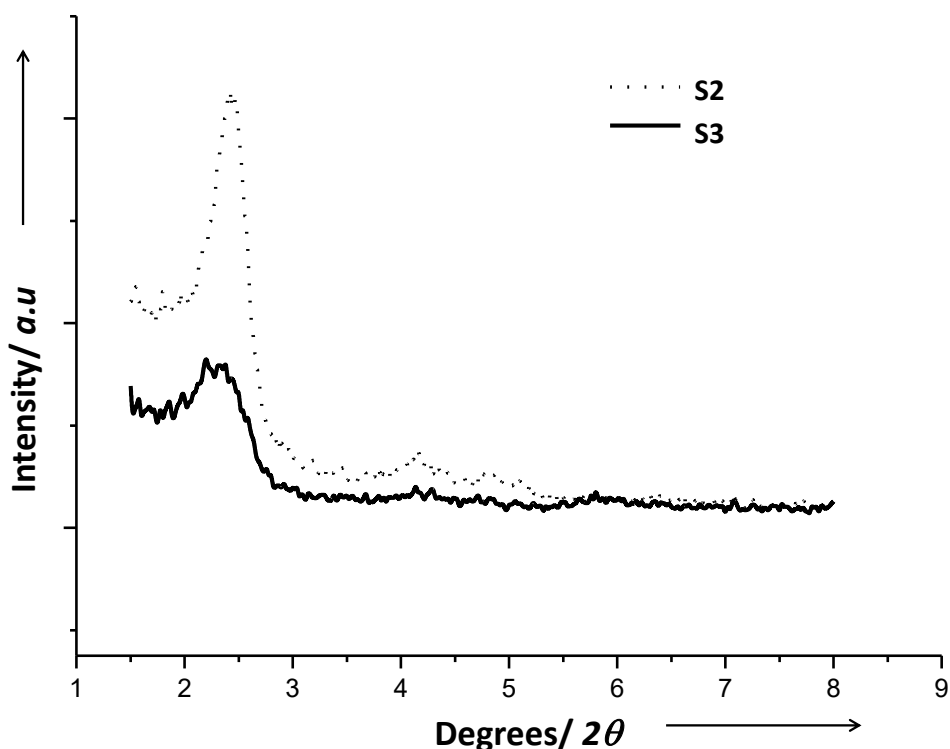
Figure SI-4. XRD pattern of **S2** nanoparticles and **S3** scaffold.

The performed thermogravimetric analysis (TGA) in the temperature range from 30ºC to 950ºC determined the percentage contents of nanoparticles and gelatin incorporated in the ink for the scaffold printing. Several samples were analyzed by TG, in order to confirm the homogeneity of the method. From this technique, a 25% ± 3.2 weight content of SiO_2 from **S2** nanoparticles was calculated. Then, from these data and **S2** organic content quantification, it can be estimated that around a 35% in weight of the **S3** scaffold is composed by **S2** nanoparticles

Kinetic studies with S2

In order to investigate the gat-ing properties of **S2** material, two samples of 4 mg of **S2** were suspended in 10 mL of water at 37 °C in the presence and in the absence of APase. The two samples were stirred at 200 rpm and then several 150µL aliquots were taken of each sample at different times. These aliquots were centrifuged at 9500 rpm and 110µL of the supernatant

was taken in order to monitor the $[Ru(bpy)_3]^{2+}$ release (λ_{ex} 454 nm, λ_{em} 593 nm) by fluorescence spectroscopy.

S3 permeability assays

An experimental assay with fluorescent avidin was carried out in order to demonstrate that the scaffold walls were permeable to macromolecules, and consequently APase could access to the MSN nanoparticles. For this assay a gelatin scaffold containing calcined MCM-41 nanoparticles (the synthesis procedure was the same than the one described for **S3** material, but containing non gated nanoparticles instead of **S2**) was immersed in a 4 mg/mL solution of fluorescent avidin in phosphate buffer solution (PBS) for 24 hours. Then, the scaffolds were intensely washed with fresh PBS in order to remove the externally adsorbed protein and cut in different levels in order to observe the fluorescence in the inner walls by fluorescence microscopy. The registered images showed fluorescence in all levels, which indicated that the scaffold walls were impregnated of avidin.

Kinetic studies with S3

In order to investigate the gating properties of **S3** material, two **S3** scaffolds were immersed in PBS solution (0.32 mL per gram of **S3**) at 37°C in the presence and in the absence of APase. The two samples were stirred at 200 rpm for 50 h and several 150μL aliquots were taken of each sample at different times. The fluorescence of the aliquots were registered (λ_{ex} 454 nm, λ_{em} 593 nm) in order to monitor the $[Ru(bpy)_3]^{2+}$ release.

Effect of the pH, the presence of other enzymes and denatured APase.

Moreover, in order to determine the selectivity of the enzymatic action of phosphatase, several studies were carried out in presence of other enzymes, such as esterase (at pH 8) or pepsin (at pH 4), with **S2** nanoparticles. Likewise, APase was denatured by heating at 70ºC for 1h, to prove that the dye delivery was produced due to the enzyme activity. It was used the same experimental procedure described above (see kinetic studies with **S2**). In **Figure SI-5** it

can be observed that satisfactorily a strong dye delivery was produced in presence of APase at pH 4.8 (curve a) compared to the low release of dye in absence of enzyme in water at pH 4.8 and at pH 8 (curves b and c) or with esterase, pepsin or denatured APase (curves d, e, f).
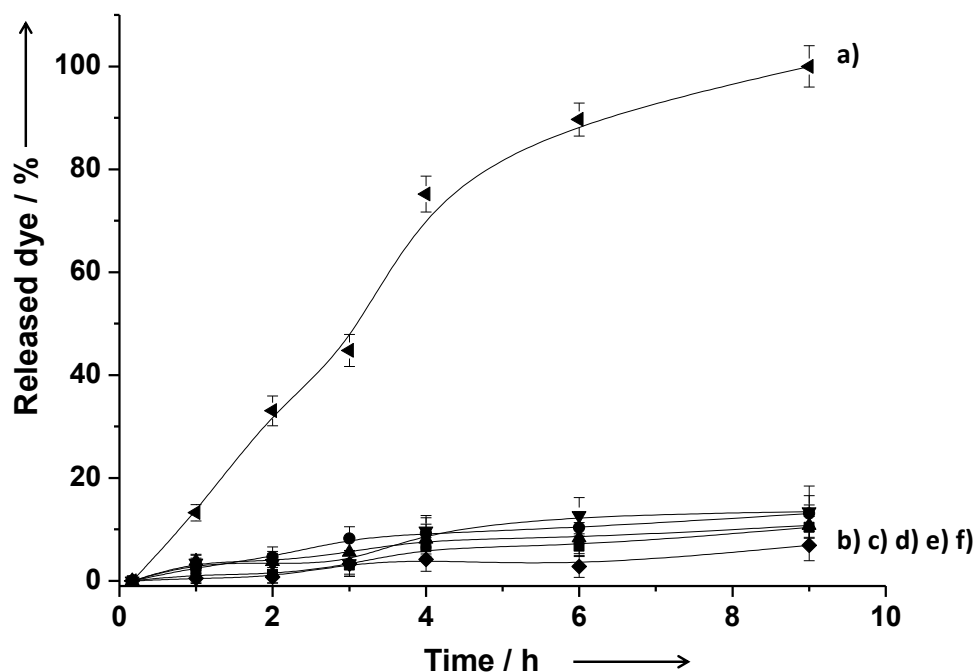

Figure SI-5. Kinetic of the dye release from **S2** in the presence of APase at pH 4.8 (a) in the absence of enzyme at pH 4.8 (b) in the absence of enzyme at pH 8 (c) in the presence of esterase at pH 8 (d) in the presence of pepsin at pH 4 (e) in the presence of denatured APase. All in water at 37ºC.

Biocompatibility studies

In order to assess the biocompatibility, *in vitro* cell culture tests were carried out on 3D gelatin framework containing silica nanoparticles. A human osteoblast-like cell line denoted HOS was used. This cell line, obtained through the European Collection of Cell Cultures (ECACC, no. 87070202), was derived from an osteosarcoma of an old Caucasian female. The cells were cultured in Dulbecco's modified Eagle medium (DMEM) containing 2 mM glutamine, 100 U/mL penicillin, 100 μg/mL streptomycin, and 10% fetal calf serum (FCS) at 37°C in a humidified atmosphere of 95% air and 5% CO_2. Osteoblast-like cells were routinely

subcultured by trypsinization. Before seeding, the scaffolds were conditioned by soaking in complete medium for 24 hours at 37ºC.

Cell proliferation assay.

For this particular assay, the cells were seeded onto the scaffolds surface in 24-well plates at a seeding density $4 \cdot 10^4$ cells·mL^{-1} in supplemented complete medium and incubated under standard conditions. Cell proliferation determinations were performed by using the MTT (3-[4,5-dimethylthiazol-2-yl]-2,5-diphenyltetrazolium bromide) assay at 3 and 5 days after seeding.

Cytotoxicity assay: Lactate deshidrogenase (LDH) activity.

LDH activity released from the osteoblast-like cells was considered for cell injury measurement. The measurements were made at 3 and 5 days of seeding by using a commercially available kit (Spinreact).

Cell-spreading assay.

The spreading degree and morphology of the osteoblast-like cells were visualized by SEM after 48 h. The attached cells were rinsed four times in PBS and fixed with 2.5% (v/v) glutaraldehyde in 0.1 M phosphate buffer. Dehydration was performed with slow water replacement by a series of graded ethanol solutions with final dehydration in absolute ethanol before critical-point drying. The materials were mounted on stubs, gold plated in vacuum using a sputter coater (Balzers SCD 004 (Wiesbaden-Nordenstadt, Germany), and analyzed by SEM in a JEOL 6400 microscope (Tokyo, Japan).

Statistics

Data obtained from biocompatibility are expressed as means ± standard deviations of the independent experiments indicated in each case. Statistical analysis was performed using the Statistical Package for the Social Sciences (SPSS) version 19 software. Statistical comparisons were made by analysis of variance (ANOVA). Scheffé test was used for post hoc

evaluation of difference among groups. In all statistical evaluations, p <0.05 was considered as statistically significant.

The results obtained from the mitochondrial activity at 3 and 5 days (**Figure SI-6**) indicate that, in the presence of the scaffolds, HOS cells proliferate even better than in the control (plastic culture plate). For the same periods, the LDH levels do not show significant differences in the presence of the scaffolds compared with the control ones, indicating that the scaffolds do not elicit any cytotoxic effect (**Figure SI-7**).
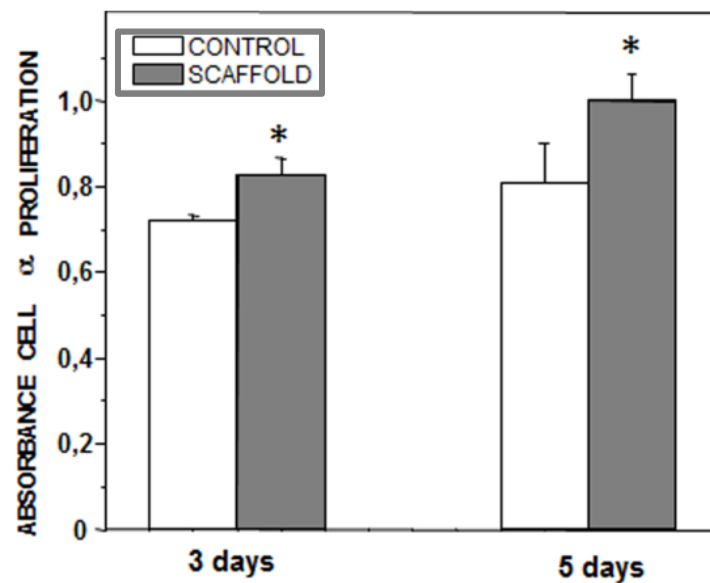

Figure SI-6. Cell proliferation assay after 3 and 5 days of culture. Significant differences were observed between the control and scaffolds results for cell proliferation tests. *(p<0.05).
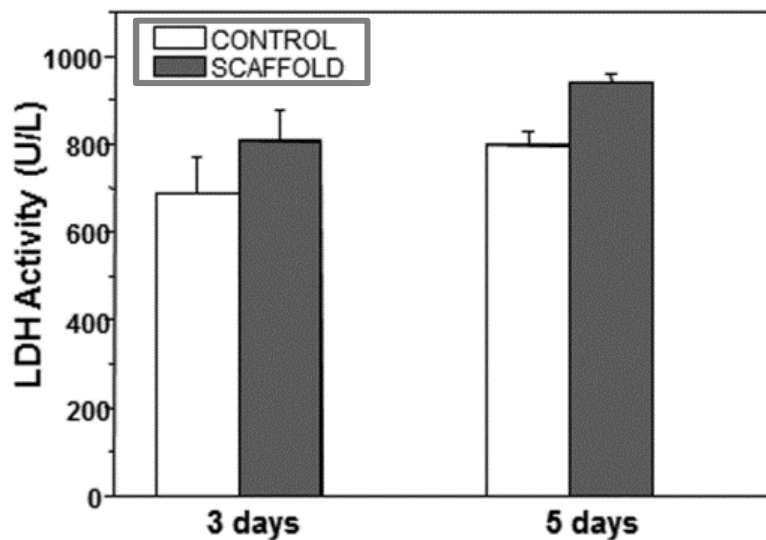
Figure SI-7. LDH activity after 3 and 5 days of culture.

HOS cells adhere, proliferate and spread well within the scaffold, as it is evidenced in SEM micrographs (**Figure SI-8**). The macroporous architecture and the strut thickness seem to be appropriated for the scaffold colonization by HOS cells. In fact, after 48 hours, the osteoblasts exhibit spread morphologies with numerous anchoring elements in both the most external and accessible surface, as well as within the macroporous channels tailored by means of the rapid prototyping method used in this work.
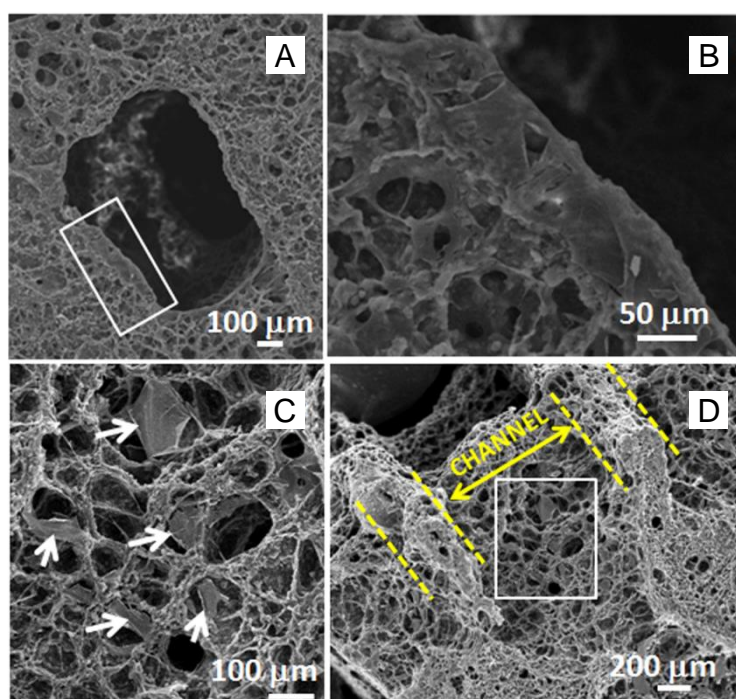

Figure SI-8. SEM micrographs of the scaffolds after 48 hours of HOS culture. (A) Detail of *c.a.* 900 μm macropore prepared by 3D printing. The selected area indicates a fully coated border site by HOS cells; higher magnification of this area (B). (C) Transversal section of the scaffolds; double arrow points the channel width and dotted lines mark the struts. The selected area is magnified in (D), where spread HOS cells can be observed (arrows).